Computers in Biology and Medicine 100 (2018) 62–73

Contents lists available at ScienceDirect

Computers in Biology and Medicine

journal homepage: www.elsevier.com/locate/compbiomed

Numerical simulation of thermal water delivery in the human nasal cavity

V. Covello[a], C. Pipolo[b], A. Saibene[b], G. Felisati[b], M. Quadrio[a,*]

[a] Department of Aerospace Science and Technology, Politecnico di Milano, Via La Masa 34, 20156, Milano, Italy
[b] Otorhinolaryngology Unit, Head and Neck Department, San Paolo Hospital, Università degli Studi di Milano, Via di Rudini 8, 20142, Milano, Italy

ARTICLE INFO

Keywords:
Thermal waters
Computational fluid dynamics
Large eddy simulation

ABSTRACT

This work describes an extensive numerical investigation of thermal water delivery for the treatment of inflammatory disorders in the human nasal cavity. The numerical simulation of the multiphase air-droplets flow is based upon the Large Eddy Simulation (LES) technique, with droplets of thermal water described via a Lagrangian approach. Droplet deposition is studied for different sizes of water droplets, corresponding to two different thermal treatments, i.e. aerosol and inhalation. Numerical simulations are conducted on a patient-specific anatomy, employing two different grid sizes, under steady inspiration at two breathing intensities.

The results are compared with published *in vivo* and *in vitro* data. The effectiveness of the various thermal treatments is then assessed qualitatively and quantitatively, by a detailed analysis of the deposition patterns of the droplets. Discretization effects on the deposition dynamics are addressed. The level of detail of the present work, together with the accuracy afforded by the LES approach, leads to an improved understanding of how the mixture of air-water droplets is distributed within the nose and the paranasal sinuses.

1. Introduction

Inflammatory disorders affecting the upper respiratory tract are among the most common conditions for which treatments with thermal waters are advised. Such treatments are typically administered as inhalations. Several thermal centers around the world offer inhalation therapy to patients, and propose natural thermal waters with different characteristics and composition. Sulfurous waters are one of the most popular choice in inhalation therapy [1,2].

Relatively recent laboratory tests have shown definite positive effects from sulfurous water, including mucolytic and trophic action on the respiratory mucosa and anti-oxidant and anti-elastase activity. Therefore, scientific evidence presently supports an anti-inflammatory action of thermal waters which effectively helps controlling the inflammatory processes of the upper respiratory tract [3–6]. Various techniques and devices have been developed to properly deliver differently fractionated thermal waters and their gaseous content to the respiratory tract: inhalations, aerosols (also in their more recent sonic/ionized variant), humages, nebulizations and nasal douches are the most common ones [1,2].

Among these, douche-based techniques, based on saline or different solutions, have a scientifically proven efficacy [7]. Irrigations and douches effectively wash the nasal cavity, although inhalations and nebulizations too do deliver water to the nasal cavity to some extent, thus providing a sort of nasal douching. It should also be noted that douches and irrigations are frequently performed in thermal centers where professional devices are available. Such devices have been demonstrated to provide a more effective delivery compared to douching performed by patients at home [8]. On the other hand, aerosols and humages do not provide douching at all, since the water delivery to the nasal cavities is minimal, and the gaseous phase largely prevails.

Even though literature studies describing the clinical effectiveness of these techniques are available, an in-depth knowledge of their details, as for example the spatial pattern of deposition of thermal water droplets over the mucosal lining of the nasal cavities, the pharynx and, broadly speaking, the upper respiratory tract is still lacking. Such knowledge would for example enable tuning and optimizing the design of thermal water diffusors for active droplets distribution, capable to target a specific district of the airway depending on the specific clinical condition. Therefore, a better understanding of the deposition pattern, and how it depends on the particular technique, combined with the type of breathing, would be useful from a clinical as well as a scientific standpoint.

A large number of *in vivo* [9–11] and *in vitro* [12–15] studies have addreseed the problem during the recent years. The difficulties in carrying out *in vivo* studies are obvious. Significant recent advances in Computational Fluid Dynamics (CFD) techniques for the study of the nasal airflow are improving the general picture, by providing a quantitative analysis tool with unprecedented analytic power. Such advances are briefly reviewed in the next section, with specific reference

* Corresponding author.
E-mail address: maurizio.quadrio@polimi.it (M. Quadrio).

https://doi.org/10.1016/j.compbiomed.2018.06.029
Received 5 March 2018; Received in revised form 24 June 2018; Accepted 25 June 2018

to the problem at hand.

The present work is an extensive numerical study, based upon the LES technique and a Lagrangian approach for tracking water droplets, of the delivery of thermal waters in a complete, patient-specific model of a human nasal cavity which includes the anatomical details of the paranasal sinuses. The study builds upon a procedure, entirely based on open-source software, which is under development by our group since some time [16–18]. The goal of the study is to describe, with a high level of detail, the process of delivery of thermal waters to the human nasal cavities. We expect our work to help improving the current understanding of how the mixture of air and droplets is distributed within the nose, and where the droplets are preferentially deposited. At the same time, assessing the effect of the main computational parameters on the deposition pattern is useful to carry out such simulations effectively and reliably. Such predictive capability is deemed to be useful for the development of next-generation thermal devices, allowing a more effective treatment of the inflammatory nasal disorders.

The paper is organized as follows. After a brief literature review presented in Sec.2, Sec.3 describes the main features of the geometrical and numerical model, and in Sec.4 the main results are presented. In Sec.5 results are discussed and compared with the literature data, and conclusions are given in Sec.6.

2. Literature review

During the last years, CFD is quickly becoming a powerful tool to investigate the physical phenomena characterizing the respiratory process, see e.g. Refs. [19–22], and more recently [23–26]. Among the most recent contributions, examples can be found in the framework of surgery planning [27,28], and for the pre- and post-surgery analysis [29–32]. Moreover, CFD is becoming a valuable research tool to drive the development and optimization of devices for the treatment of inflammatory disorders [33–36].

Several CFD studies have been devoted to assessing the efficiency of droplet deposition in the human nasal cavity, by comparing the behavior of different types of droplets in different anatomies. Many of them consider the nasal airflow to be laminar [37–42]; others classically solve the Reynolds-Averaged Navier–Stokes equations (RANS), where turbulence effects are indirectly accounted for through a suitable turbulence model. In particular, different studies have employed the so-called $k-\omega$ model [43–50]. Few are the studies employing the Large Eddy Simulation technique (LES), which implies larger computational costs compared to RANS, but brings about a potentially higher fidelity of the results; despite its widespread use within the CFD community at large in a vast range of applied problems, LES is not routinely employed yet in computational studies of the nasal airflow. Moreover, the existing examples [44,51–56] often consider simplified or idealized anatomies, excluding the anatomical details of the frontal and maxillary sinuses, despite their importance for the treatments of many inflammatory disorders.

3. Methods

The numerical simulation of the two-phase air-droplets flow in the reconstructed nasal cavities of an anatomically normal subject is performed by means of the open-source CFD software OpenFOAM [57]. The three-dimensional computational domain is reconstructed, according to the procedure illustrated in Ref. [16], from a CT scan via the open-source software package 3D-Slicer [58]. The snappyhexmesh utility available in OpenFOAM is used for the generation of the volume mesh where the equations of motion are discretized, and OpenFOAM itself is used for the actual numerical solution of the discretized equations in the LES framework and for tracking the water droplets.

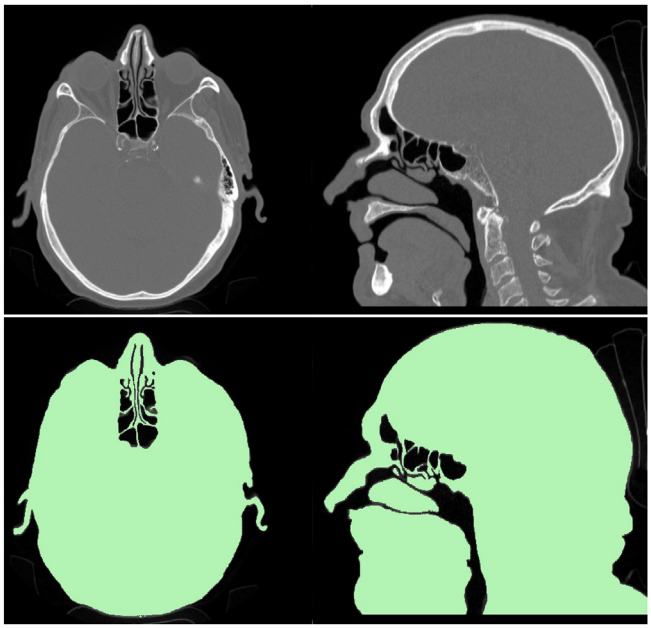

Fig. 1. Representative CT images (top) and their segmentation obtained with a threshold value of $HU = -218$ (bottom), after removal of the connection between epiglottis and mouth. Black regions correspond to the air-filled volume.

3.1. The geometrical model

The procedure starts with an accurate reconstruction of the anatomy of the upper airways, including nasal sinuses, from a standard CT scan. After approval by the internal Institutional Review Board (IRB) of the San Paolo Hospital, University of Milan, the scan of a 67-years-old male presenting a normal sinonasal anatomy was selected. The whole CT scan contains 348 DICOM images; in each image the spatial resolution is 0.5 mm × 0.5 mm in the sagittal–coronal directions, and a 0.6 mm axial gap separates consecutive slices. 3DSlicer [58] is used to convert the CT images into an accurate geometrical model of the bone-air boundary by means a proper choice of a radio-density threshold.

Fig. 1 shows a sample of the original CT images, encoded in grayscale, and the same image after the segmentation process, carried out with a threshold of $HU = -218$ Hounsfield units. This particular HU value is selected to yield the best anatomical reconstruction as judged from expert ORLs. For further discussion on this fundamental step of the procedure see e.g. Ref. [18]. The reconstructed three-dimensional geometry is then exported into a STereoLithography (STL) file, to be used as input for the subsequent steps. As our interest is focused on the nasal region, the connection between epiglottis and mouth and the pyriform sinuses have been removed from the STL model.

The model is complemented with an external air volume, where the droplets to be inhaled are uniformly distributed at the beginning of the simulation. To this aim, the STL anatomical surface is intersected with a carefully placed external spherical volume placed around the nostrils. As shown in Fig. 2 (left), the union of the sphere and the inner airways constitutes the computational domain proper. Size and position of the sphere are designed to minimize the computational overhead while at the same time still providing an high-quality mesh. The snappyHexMesh utility is then used to generate a computational finite-volumes mesh from the complete STL file. The quality of the mesh has been carefully assessed with both non-orthogonality and skewness criteria, by using a max orthogonality angle of 60° and imposing a max skewness of 4 and 6, for the boundary and the internal face, respectively. Fig. 2 (right) shows the final STL model, the whole computational domain for a mesh with approx. 25×10^6 cells (the finest mesh employed here), with emphasis on two representative sagittal and coronal sections.

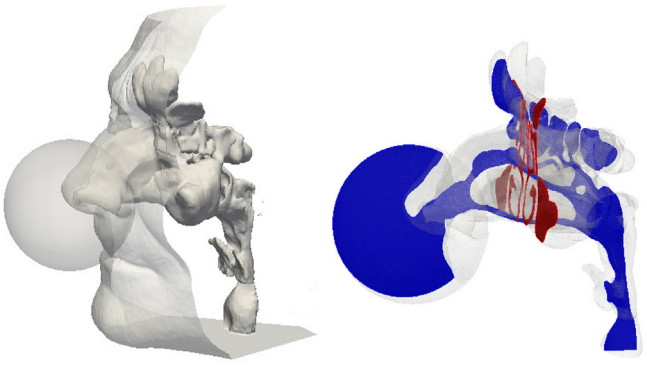

Fig. 2. Left: the whole computational domain, made by the inner airways plus the outer spherical volume. Right: sagittal (blue) and coronal (red) sections, showing the volume mesh for the finest mesh employed in this work, made by approximately 25 M cells. (For interpretation of the references to color in this figure legend, the reader is referred to the Web version of this article.)

3.2. The mathematical model

3.2.1. Air

The governing equations expressing conservation of mass and momentum balance for the continuous phase (i.e. air) are the incompressible Navier–Stokes and continuity equations:

$$\nabla\cdot\mathbf{u} = 0 \tag{1}$$

$$\frac{\partial\mathbf{u}}{\partial t} + (\mathbf{u}\cdot\nabla)\mathbf{u} - \nu\nabla^2\mathbf{u} + \frac{\nabla p}{\rho} = 0 \tag{2}$$

in which $\mathbf{u}$ denotes the velocity vector, p is pressure, ρ the (constant) density, and ν the kinematic viscosity.

According to the LES approach [59], the filtered form of the governing equations is used:

$$\nabla\cdot\,\widetilde{\mathbf{u}} = 0 \tag{3}$$

$$\frac{\partial\widetilde{\mathbf{u}}}{\partial t} + (\widetilde{\mathbf{u}}\cdot\nabla)\widetilde{\mathbf{u}} - \nu\nabla^2\widetilde{\mathbf{u}} + \nabla\cdot\tau_{sgs} + \frac{\nabla\bar{p}}{\rho} = 0 \tag{4}$$

where the decomposition $\mathbf{u} = \widetilde{\mathbf{u}} + \mathbf{u}'$ is introduced, the symbol $\widetilde{\ }$ denotes the filtered (or resolved) component, a prime denotes the subgrig-scale (SGS) component, and τ_{sgs} is the subgrid stress tensor.

In the present work, emphasis is not placed on the choice of the specific subgrid turbulence model. In fact, the employed meshes are typically quite fine; as a consequence, the contribution of the subgrid model is of modest importance, as shown later on. Hence, τ_{sgs} is modelled via the simplest and cheapest available model, i.e. the static Smagorinsky model [60]:

$$\tau_{sgs} = -2\nu_{sgs}\widetilde{D}. \tag{5}$$

The above expression specifies the tensor τ_{sgs} as proportional to the strain tensor $\widetilde{D}$ of the filtered velocity field, defined as $\widetilde{D} = \frac{1}{2}(\nabla\widetilde{\mathbf{u}} + \nabla\widetilde{\mathbf{u}}^T)$, via a scalar function ν_{sgs}, the so-called subgrid eddy viscosity, taken as:

$$\nu_{sgs} = \ell_s^2\widetilde{S} = (C_s\Delta)^2\widetilde{S}$$

in which $\widetilde{S}$ is the characteristic filtered rate of strain, $\widetilde{S} = (2\widetilde{D}\colon\widetilde{D})^{1/2}$, and ℓ_s is the Smagorinsky lenghtscale, assumed to be proportional via the Smagorinsky coefficient $C_s \approx 0.17$ to the filter width Δ. This quantity, defined as $\Delta = (\Delta x\Delta y\Delta z)^{1/3}$, in which Δx, Δy, Δz are the grid spacing in the three spatial directions, is a length scale associated to the size of the computational grid. To avoid non-zero values of ν_{sgs} at solid boundaries, we use a van Driest damping function [61] to specify ℓ_s as $\ell_s = f_d C_s\Delta$, in which f_d stands for the damping function, varying along the wall-normal direction.

3.2.2. Droplets

For the dispersed phase, the motion of the water droplets is described by means of a Lagrangian approach. Due to the very low volume fraction occupied by the droplets, that never exceeds 0.1% and is often much lower, droplets are assumed to possess a one-way coupling to the velocity field, as discussed in Ref. [62], i.e. their dynamics is affected by the flow, but not vice-versa. Position and velocity of each droplet are computed by a set of differential equations where droplets are considered as rigid spheres, neglecting heat and mass transfer. As every droplet is a simple point mass, its dynamics is expressed as:

$$\frac{d\mathbf{x}_p}{dt} = \mathbf{u}_p,$$

$$m_p\frac{d\mathbf{u}_p}{dt} = \Sigma\mathbf{F}_i,$$

where $\mathbf{x}_p$ is the position vector of the droplet, $\mathbf{u}_p$ is its velocity and m_p is its mass. The term $\Sigma\mathbf{F}_i$ expresses the sum of all the relevant forces acting on the droplet, and includes the dependence on the fluid velocity. In the present study, we only consider 3 forces: $\mathbf{F}_D$, the drag force exerted on the droplet by the continuous phase; $\mathbf{F}_B$, the buoyancy force; and $\mathbf{F}_G$, the gravitational force. Due to the small air-droplets density ratio equal to $\approx 10^{-3}$, and the low flow acceleration rate, these three forces alone influence the droplet dynamics, while other forces, such as the Basset history term, can be safely neglected [62].

The total drag force experienced by a droplet is expressed as:

$$\mathbf{F}_D = \frac{3}{4}\frac{\rho}{\rho_p}\frac{m_p}{d_p}C_d(\mathbf{u}-\mathbf{u}_p)\left|\mathbf{u}-\mathbf{u}_p\right|$$

where d_p is the droplet diameter, and ρ_p is its density. The drag coefficient C_d depends upon the flow regime, and is a non-linear function of the Reynolds number $Re_p = \rho d_p(\mathbf{u}_p - \mathbf{u})/\mu$ based on droplet diameter and the relative velocity. Here we employ the following empirical relationship valid for spherical particles [62]:

$$C_d = \frac{24}{Re_p}\left(1 + \frac{1}{6}Re_p^{2/3}\right);\ Re_p \le 1000. \tag{6}$$

Since for the cases considered in the present work Re_p ranges from 10^{-2} to 1, the expression above is not too far from the laminar law $C_d = 24/Re_p$.

Finally, the buoyancy and gravitational force are defined together as:

$$\mathbf{F}_B + \mathbf{F}_G = \frac{(\rho_p - \rho)\pi d_p^3}{6}\mathbf{g}.$$

where $\mathbf{g}$ is the gravitational acceleration.

3.3. The computational setup

The LES cases considered in the present work describe the steady inhalation of water droplets suspended in air, for a total duration of 0.6 s.

The discretized version of the governing equations for air is solved with the stock finite-volumes OpenFOAM solver pimpleFoam, which is based on a mixed PIMPLE-PISO approach for the pressure-velocity coupling [63]. The discretized equation that computes the trajectories of the droplets is coupled to the equations of the continuum phase by means of the OpenFOAM function object icoUncoupledKinematicCloud. All the numerical simulations are performed with fully second-order discretization schemes in space and time.

The boundary of the computational domain is split into three portions, where different boundary conditions are applied: the outlet section at the throat, the inlet section at the outer surface of the spherical region outside the nose, and the whole mucosa-lined surface of the internal nasal cavities. Air and droplets are driven through the system

by an imposed pressure difference Δp between inlet and outlet, i.e. between the external ambient and the throat, as done e.g. in Ref. [64]. Two values of Δp, namely $\Delta p = 10$ Pa and $\Delta p = 20$ Pa are considered in the present work, with $p = 0$ at the inlet and total pressure set at -10 Pa or -20 Pa on the outlet. This yields flow rates of approx. $Q = 13$ L/min and $Q = 20$ L/min. Such flow rates are typical of low- and medium-intensity physical activity [38,65–67]. The boundary conditions for the velocity vector are homogeneous Dirichlet (i.e. no-slip) on the mucosa, treated as a solid wall, and homogeneous Neumann at the outlet. On the inlet surface, i.e. the outer surface of the spherical region, an homogeneous Neumann boundary condition for the normal velocity component is used, and an homogeneous Dirichlet for the tangential component. An homogeneous Neumann condition for turbulent viscosity is used everywhere but on the mucosa, where ν_{sgs} is set to zero. Initial conditions for the velocity and pressure fields are trivially set to zero, with the turbulent viscosity equal to the molecular viscosity. Before the simulation proper is run and droplets are placed in the flow field, a preliminary simulation brings the flow to a statistically steady solution. As far as droplets are concerned, their velocity is set to zero whenever they reach the mucosa and stick to it, by imposing a Dirichlet boundary condition. On the outlet surface, i.e. the throat section, the outgoing droplets are removed from the computation as soon as they cross the boundary. At the initial time droplets are placed in the spherical volume with zero velocity, and quickly adapt to the steady outer flow field, where velocity magnitude is minimal. To some extent, this represents an approximation, but the flow conditioning properties of the nasal valve render the present approach significant for all those cases where an inhaler is not used.

The calculations start from developed velocity and pressure fields, and are advanced in time with a time step of 5×10^{-5} sec. This choice descends from a balance between the accuracy of the (implicit) second-order temporal integration scheme and computational cost. Time steps ranging from $O(10^4)$ to $O(10^6)$ are indeed generally reported in the literature for simulations involving mesh size with millions of cells [44,55,68]. At $t = 0$ more than 10^5 droplets are placed into the spherical volume of the computational domain and then followed during their evolution. The number of droplets inserted at $t = 0$ has been determined by extrapolating data available in the literature, see e.g. Refs. [69–71], and is meant to reproduce as closely as possible the droplets inhalation rate obtained with medical devices. In particular, the number of droplets is 2.5×10^5 for aerosol, and 3.2×10^5 for inhalation.

Two mesh sizes (with approximately 8×10^6 and 25×10^6 cells) are considered, to investigate potential effects of the discretization on deposition statistics. Moreover, three different droplet sizes are considered, with diameter d_p of 5, 10 and 50 μm. The first two values are representative of the average diameter of water droplets for aerosol and inhalation, respectively [1]. The largest value, that corresponds to the droplet size of the atomized nasal douche, is given here for reference purposes only.In fact, although the initial droplet density is matched to the actual device in this case too, it is important to point out that here the water droplets are at rest at the beginning of the simulation. This is an acceptable hypothesis for the smaller droplets, but becomes questionable if the largest ones are to be connected with the nasal douche. Indeed, in the atomized nasal douche the droplets are usually injected into the nasal cavity with a strong velocity by using thermal devices [1,2]. As a consequence, the deposition statistics for the largest droplets should be interpreted with care, and their link to the treatment of atomized nasal douche is qualitative only, although they provide a qualitative idea of the behavior of larger particles that might be produced by some inhalation devices.

The entire set of simulations is composed by 14 cases summarized in Table 1. For convenience, each computational setup is identified by a three-letters acronym according the following rules: l = low (10 Pa) or high (20 Pa) pressure drop; a = aerosol, i = inhalation, d = atomized nasal douche; c = coarse mesh, f = fine mesh. Two additional cases with the fine mesh, labeled haf- and haf+, are carried out to explore the effect of spatial resolution in the near-wall region via an increase/decrease of the number of near-wall cells while the global mesh size is kept at 25 M.

Table 1
List of the numerical simulations.

Case	Δp	Particle	Grid size
	[Pa]	Diameter [μm]	[M cells]
lac	10	5	8
lic	10	10	8
ldc	10	50	8
hac	20	5	8
hic	20	10	8
hdc	20	50	8
laf	10	5	25
lif	10	10	25
ldf	10	50	25
haf	20	5	25
haf-	20	5	25
haf+	20	5	25
hif	20	10	25
hdf	20	50	25

All numerical simulations have been performed on the Galileo system (2 8-cores Intel Haswell processor per node, running at 2.40 GHz) of the CINECA supercomputing center, by using 32 to 96 processors. The computational cost of the entire study is approximately 40000 CPU hours. The whole computational procedure presented in this work is efficient enough for us to consider $O(10^5)$ droplets with a negligible computational overhead, even on the smallest mesh size, when compared to the single-phase simulation alone. Increasing the mesh size decreases the relative overhead further, as the lagrangian calculations do not see their cost increase with the mesh size.

4. Results

In this section the results of our computational study are presented. In a first step, a general description of the solution is provided, where the velocity and pressure fields of the continuous phase are described for the most computationally demanding case (largest mesh and highest flow rate). Next, the way droplets are deposited across the nasal cavity and the paranasal sinuses is addressed; lastly, results are expressed in terms of deposition fraction, and the effects of the various parameters at play, either physical or discretization-related, are described.

4.1. Velocity and pressure fields

In this section some general features of the solution are described, with reference to the case with the largest mesh and the highest flow rate (cases h*f in Table 1).

It is well know that LES simulations produce time-dependent results. In the following the key features of the time-averaged velocity and pressure fields are described, as well as those of derived vector fields like the time-averaged vorticity field. Moreover, once the time-average is known, fluctuations around the mean value can be computed, to provide a statistical indication of the fluctuating character of the flow in terms of variances. We indicate the time-averaged fields with an overbar, so that e.g. $\overline{\mathbf{u}}$ is the time-averaged velocity vector. Averages and variances of fluctuating quantities are computed runtime by accumulating them during the simulation.

In Fig. 3 contours of the mean pressure $\overline{p}$ (top) and the mean velocity magnitude $|\overline{\mathbf{u}}|$ (bottom) fields are plotted. The two sagittal (left) and coronal (right) sections already highlighted in Fig. 2 are represented. In the sagittal view, the largest velocity values, about 5 m/s, are observed to occur close to the throat region, as a consequence of the reduction of the cross-sectional area. It can be appreciated that considerably large values occur in the meati region too, where the velocity

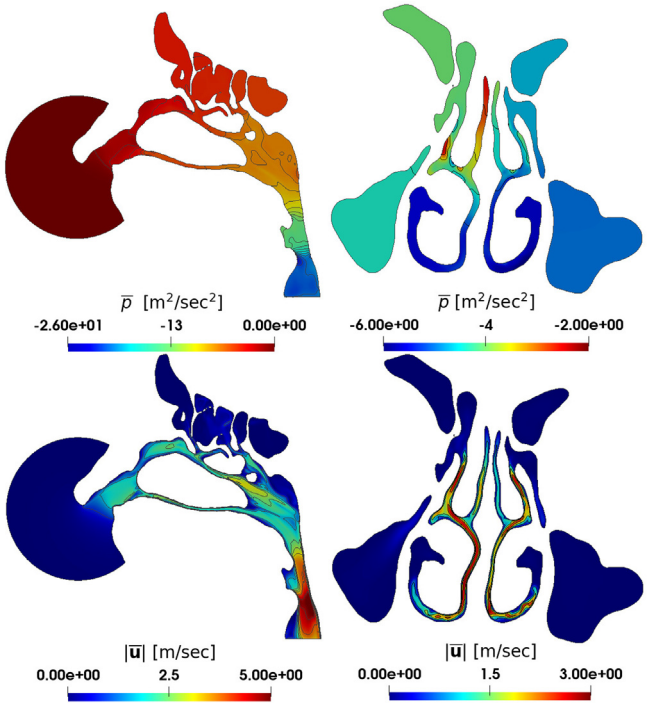

Fig. 3. Contours of the mean pressure field (top) and of the magnitude of the mean velocity (bottom), shown in the same sagittal (left) and coronal (right) sections visible in Fig. 2. Isoline increment is 0.7 m/s for velocity, and 1.0 m^2/sec^2 for pressure.

magnitude reaches about 3 m/s. Moreover, particularly in the sagittal section, low but definitely non-zero mean velocity levels in some of the ethmoidal cells are observed. The sagittal section highlights how the mean pressure gradually decreases along the airways, reaching its minimum in the throat region. Indeed, the true minimum takes place just beneath the larynx. Note that the lowest value of pressure is observed downstream of the epiglottis, and slightly exceeds the imposed global $\Delta p = 20$ Pa. A look at the mean pressure in coronal view presents an asymmetrical behavior, with larger pressure values on the left side; similar observations can be drawn by looking at the velocity contours. A more detailed, component-wise description of the mean velocity field is given in Fig. 4, w.r.t the sagittal (first column) and coronal (second column) sections, for the $\overline{u}$ (top row), $\overline{v}$ (middle row), and $\overline{w}$ (bottom column) component. The largest values, about 5 m/s, are observed for the vertical $\overline{w}$ component close to the throat section. Large velocity values also occur for $\overline{v}$, about -3 m/s, in the meati region. Furthermore, the presence of the small but non-zero velocity is evident for all the components in the volume of the paranasal sinuses.

Besides the mean flow field, with a LES one can easily access the variance of velocity fluctuations, quantities that in a RANS-based simulation are completely left to the model equations, and often not distinguished from the turbulent kinetic energy, thus missing the anisotropic character of the flow. In Fig. 5 the turbulent kinetic energy, i.e. the kinetic energy of the fluctuating velocity field, as reconstructed from the variance of the velocity components is illustrated, by plotting it on the same sagittal and coronal sections of the previous figure. We notice the largest values of the turbulent kinetic energy downstream the epiglottis in the sagittal section, where the kinetic energy reaches up to 1.8 m^2/sec^2, thus pointing to an highly 3-dimensional flow.

The shear layer detaching from the epiglottis, which can be observed in the field of turbulent kinetic energy, is much better visualized on the next Fig. 6, which focuses on the regions of the flow field with large velocity gradients by plotting contours of the vorticity magnitude $|\omega|$. Besides the high values near the wall, related to the wall gradient of the mean and instantaneous velocity field, the sagittal section

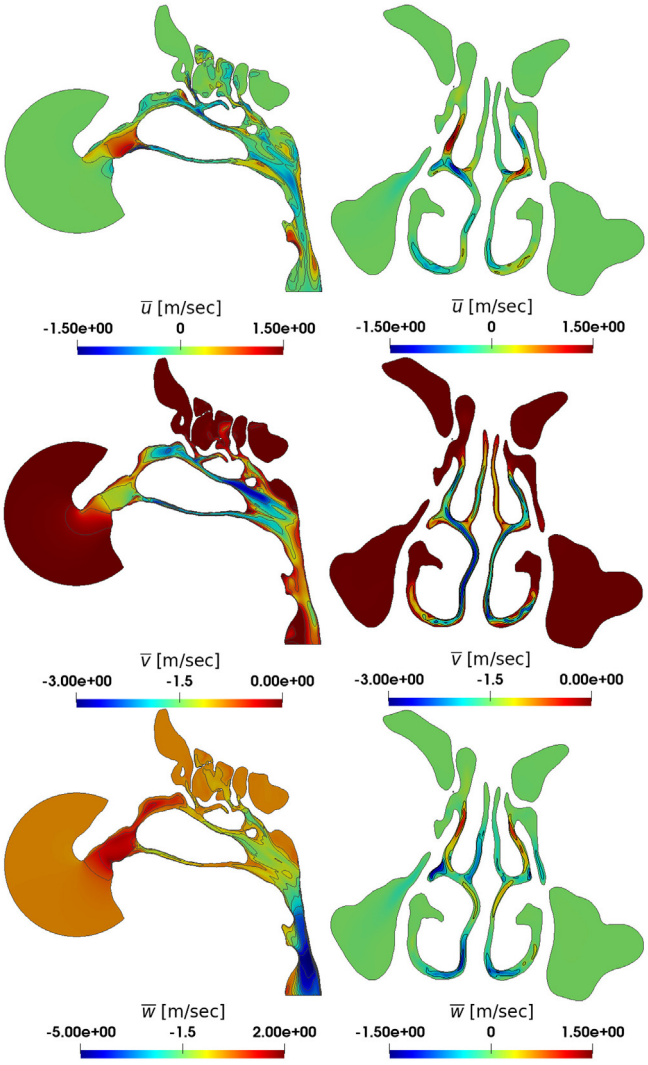

Fig. 4. Contours of the mean velocity field in sagittal (left) and coronal (right) sections; $\overline{u}$ component (top), $\overline{v}$ component (center), $\overline{w}$ component (bottom). Isolines increment is 0.5 m/s.

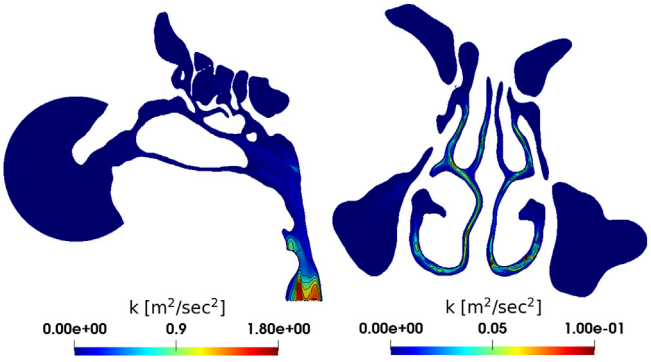

Fig. 5. Contours of the turbulent kinetic energy in sagittal (left) and coronal (right) sections; Isoline increments by 0.25 m^2/sec^2 and 0.02 m^2/sec^2 in the sagittal and coronal views, respectively.

emphasizes the strong shear layers in the bulk flow. They appear to detach both from the nasal concha in the nasopharynx, and from the epiglottis in the throat region. The two magnified views in the lower part of Fig. 6 highlight the recirculation region close to the nasopharynx and the development of a shear layer downstream of the epiglottis.

An alternative and perhaps more significant view of the vortical

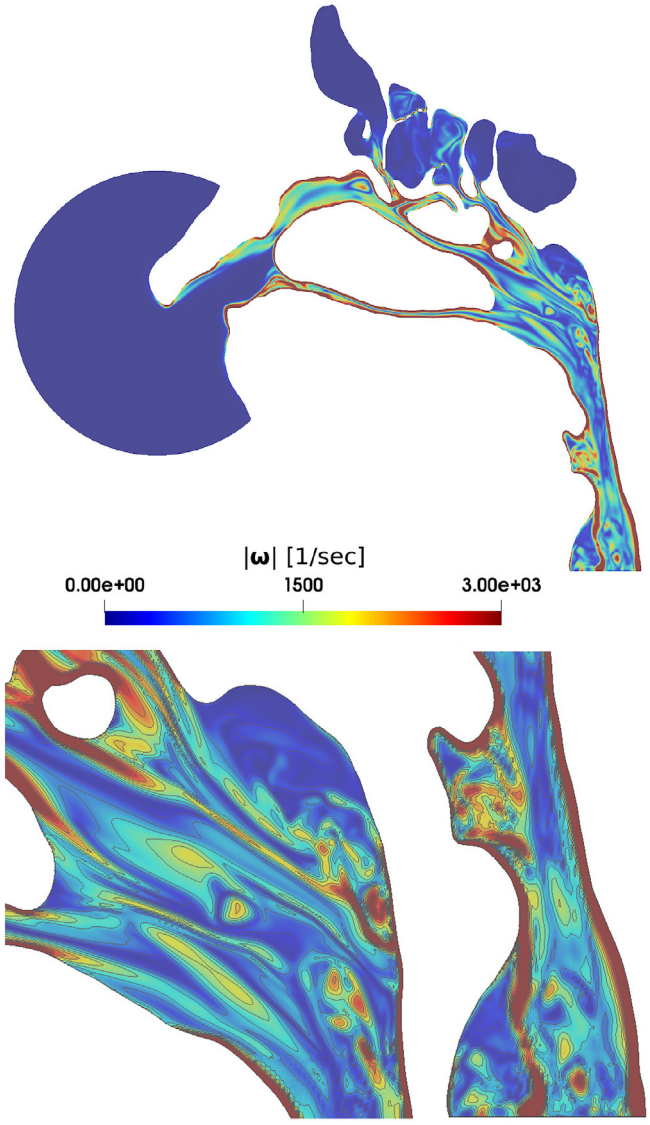

Fig. 6. Magnitude of the vorticity field. Top: sagittal section. Bottom: same section, with zoom on the nasopharynix (left) and on the larynx (right) regions. Isolines every 333.0 sec^{-1}.

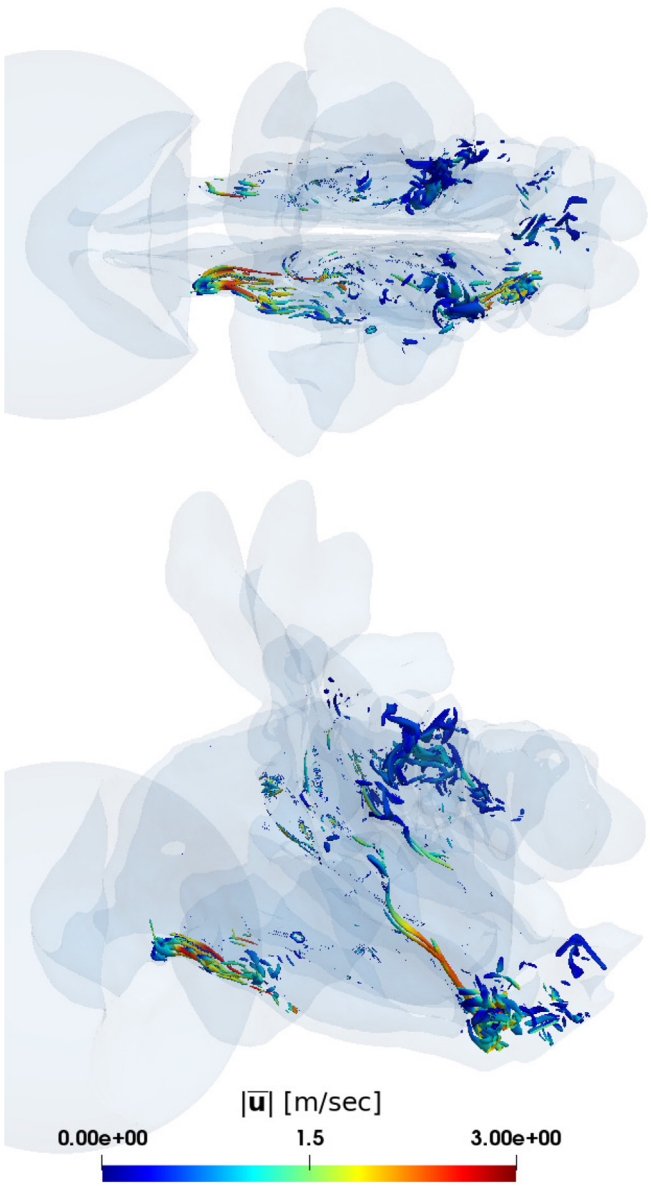

Fig. 7. Isosurface for $\lambda_2 = 60000\ sec^{-2}$ in an instantaneous velocity field, after 0.2 s of inspiration, colored by the value of the local velocity magnitude. Top: axial view; bottom: prospective view.

structures in the flow is proposed in Fig. 7, where the focus is on the upper region of the nasal cavity. Here we plot, for an instantaneous flow field, an isocontour of the scalar quantity λ_2, which is defined as the intermediate eigenvalue of the velocity gradient tensor, and is often used to highlight [72] the presence of vortices. λ_2 is computed by subtracting the mean velocity field from the instantaneous one. The figure features an axial (top) and a perspective (bottom) view, in which the mucosa is shown in transparency. The λ_2 isosurface is colored according to the magnitude of the local velocity vector. The structures present along the meati, and especially the inferior meatus, are clearly convected away by a relatively large velocity. Moreover, the perspective view emphasizes the recirculation region close to the nasopharynx, where intense vortical structures reside. In both views some evidence of λ_2-identified vortical structures is observed for the paranasal sinuses, especially in the region of the ostii, although the structures are characterized by low values of local velocity.

4.2. Droplet deposition

The process of deposition of droplets of thermal water upon the nasal mucosa is now assessed, both qualitatively and quantitatively, for the entire set of simulations reported in Table 1. In Fig. 8 the spatial distribution of the liquid droplets deposited on the nasal mucosa is represented, by visualizing with a blue dot every droplet that, during the duration of the simulation, ends up sticking to the mucosal lining. Of all the droplets present at the beginning of the simulation, those that have exited through the outflow as well as those that are still in flight at the end of the simulation are not plotted. The two cases considered, both for the finest mesh with the largest pressure difference, are the two extrema of the smallest droplets (aerosol) and the largest one (loosely corresponding to the atomized nasal douche) (cases haf, hdf in Table 1). The mucosal lining is shown with partial transparency, and colored by the value of the mean pressure $\overline{p}$.

The most striking difference between the deposition pattern of the two droplet sizes is the extent of the region reached by droplets. The finer aerosol particles appear to spread over the entire mucosal lining, from the anterior part of the nose up to the throat region, with prevalence for the nasal concha and the region between nasopharynx and throat. Conversely, the large droplets with 50 μm diameter are all

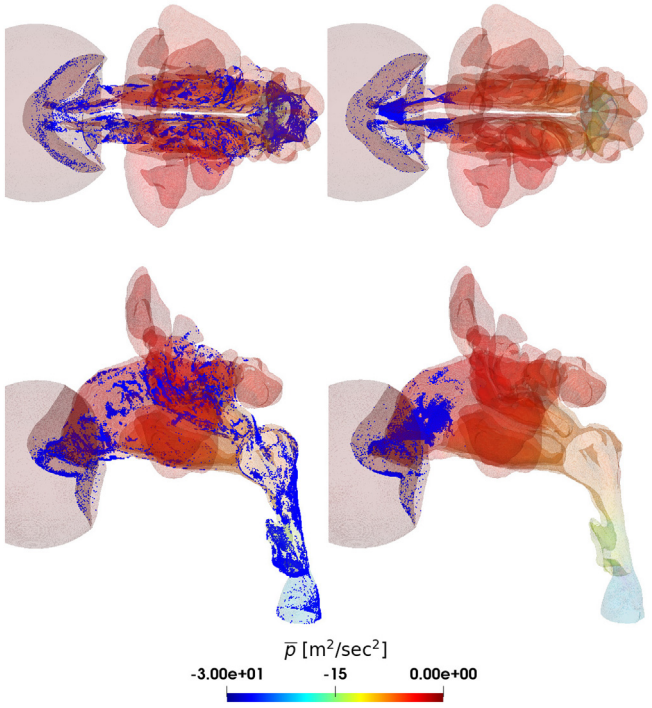

Fig. 8. Axial (top) and sagittal (bottom) views of droplets deposition: every blue dot represents a droplet that has been deposited to the mucosa. Left: droplets with 5 µm diameter (aerosol); right: large droplets with 50 µm diameter. (For interpretation of the references to color in this figure legend, the reader is referred to the Web version of this article.)

deposited just downstream the nostrils and at the beginning of the nasal concha. In both cases, the particles injected on the spherical volume are roughly 2×10^5. At the end of the simulation, i.e. after 0.6 s, 1.6×10^5 particles have been inspired and 8.3×10^4 deposited on the mucosa for the aerosol, whereas 8.8×10^4 of the largest droplets have been inspired, but they are completely deposited.

In order to perform an extensive quantitative analysis and to compare with literature data, the entire surface of the internal nasal cavity has been subdivided in 43 consecutive slabs, as shown in Fig. 9, where,

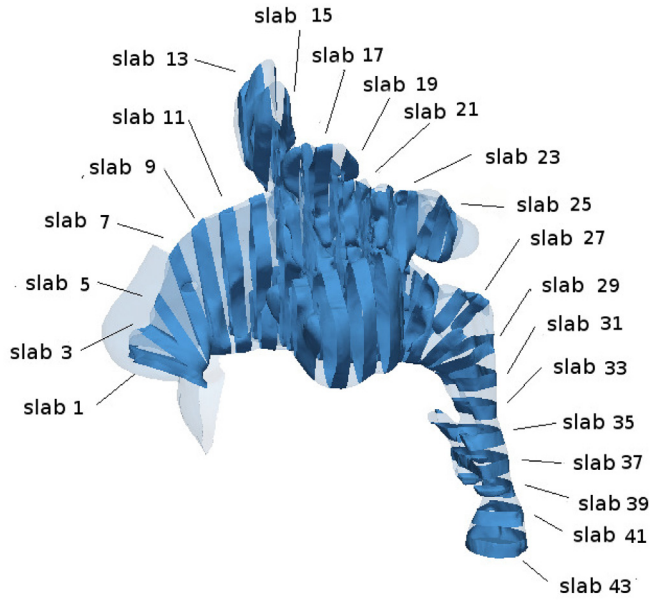

Fig. 9. Partition of the internal surface of the nasal cavity into slabs. For clarity, only the odd slabs are drawn.

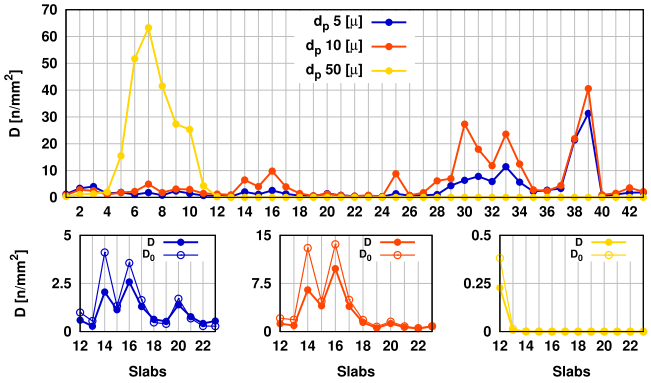

Fig. 10. Density D_i of droplets deposited upon slab i, for $\Delta p = 20$ Pa. Top: variation of D_i along the whole nasal cavity, in dependence of the thermal treatment. Bottom: differences between D_i and $D_{i,0}$ (sinuses removed), for droplet diameter of 5μm (aerosol, left), 10 µm (inhalation, center) and 50 µm (right).

for clarity, only the odd slabs are drawn. Each slab is defined within the Paraview visualization software [73], by means of two consecutive cutting planes; the thickness of each slab is approximately 5 mm, and the orientation of the cutting planes is such that every slab is approximately normal to the local axis of the nasal passageway. Various statistical quantities are then examined after volume or surface integration over each slab, to assess their variation along the main airway axis.

The surface density of droplets deposited upon the external contour of each slab is considered first. The density D_i in slab i is defined as:

$$D_i = \frac{P_i}{A_i},$$

where P_i denotes the number of particles deposited on the mucosal lining in slab i, and A_i is the slab area, expressed in mm^2. Since slabs from 11 to 23 include portions of the sinuses, for them we can additionally compute the droplet density over the mucosa of the nasal concha only, by excluding the sinuses. This is defined as $D_{i,0} = P_{i,0}/A_{i,0}$, where the additional subscript 0 indicates quantites computed excluding the sinuses, and $A_{i,0} < A_i$ for $12 < i < 23$.

Fig. 10 compares the behaviour of the deposited droplets per unit area for all the treatments (cases haf, hif, hdf in Table 1). The first row shows how D_i changes over the entire nasal cavity, whereas on the second row a close comparison of D_i vs $D_{i,0}$ is presented for each droplet size, only in the portion of the passageway where the slabs contain paranasal sinuses. In agreement with the qualitative observations put forward for Fig. 8, for the largest droplets the deposition occurs almost entirely in the small anterior region contained between slabs 5 and 11, with densities D_i ranging from about 10 to 64 mm^{-2} and being up to 10 times larger than those typical of the other treatments.

Conversely, for the smaller droplets corresponding to aerosol and inhalation, droplet deposition tends to occur over the entire domain. Indeed, the largest densities are observed over the region downstream the nasopharynx, approximately from slabs 28 to 39. For both treatments, maxima of about 30–40 droplets per mm^2 are observed on slabs 38–39. Aerosol and inhalation appear as qualitatively similar, if exception is made for slabs 14–17, corresponding to the anterior part of the nasal concha, and for slabs 28–31, 33–35 and 38–39 downstream the nasopharynx, where inhalation shows densities 2–5 times larger than those of aerosol.

Focusing now on the paranasal sinuses, we observe that for each treatment $D_{i,0} > D_i$ almost everywhere, indicating that, as expected, globally deposition on the nasal concha prevails over that in the sinuses, but the latter is non-negligible. In slabs 18, 19, and 21–23, however, $D_{i,0} < D_i$ is observed for aerosol. Droplets densities in the sinuses-related region for aerosol are more uniform along the slabs than

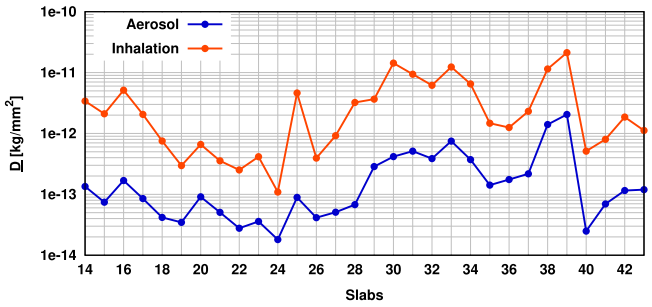

Fig. 11. Mass-weighted density $\underline{D}_i$ for aerosol and inhalation droplets, at $\Delta p = 20$ Pa. Note the logarithmic scale of the vertical axis.

those for inhalation, and for the largest droplets they are zero almost everywhere, except on slab 12 where D_{12} and $D_{12,0}$ are about 0.22 and 0.38 mm^{-2} respectively. The largest densities for aerosol and inhalation occur on slab 14 and 16, where major differences between D_i and $D_{i,0}$ are observed: densities are about 2.0, 4.0 mm^{-2} and about 6.0, 13.0 mm^{-2} for the aerosol and inhalation on the slab 14, respectively, and about 2.5, 3.5 mm^{-2} and 10.0, 13.5 mm^{-2} for the aerosol and inhalation on the slab 16, respectively.

In Fig. 11 an alternative assessment for the droplet density is proposed, focusing on the area ranging from slabs 14 to 43, for aerosol and inhalation. The droplet density has been assessed as $\underline{D}_i = M_i/A_i$, in which M_i stands for the total mass of droplets deposited in the slab i, expressed in kg and calculated as $M_i = mP_i$, where m denotes the mass of a single particle. Fig. 11 shows a qualitatively similar behaviour for aerosol and inhalation, but the inhalation droplet density is approximately one order of magnitude larger than the aerosol one, quite consistently along the entire nasal passage.

To quantitatively assess the effect of the breathing regime on the surface particle density, in Fig. 12 the statistics of Fig. 10 are reproduced for the lower breathing rate driven by a pressure difference of $\Delta p = 10$ Pa, i.e half the pressure difference (cases laf, lif, ldf in Table 1). The behaviour of D_i is quite similar, but the number of deposited droplets per unit area is generally much smaller. The largest density values for aerosol and inhalation are 20–50 mm^{-2}, in slabs 38–39. Only in these slabs, differences between inhalation and aerosol are higher than the previous case at $\Delta p = 20$ Pa. Over the region downstream the nasopharynx, from slabs 27 to 37, the aerosol particle density reaches values up to about 4 mm^{-2}, whereas the inhalation up to about 15 mm^{-2}, moreover the differences between such treatments are smaller than in the previous case with $\Delta p = 20$ Pa. We point out that over the entire mucosa D_i for inhalation is larger than that for aerosol,

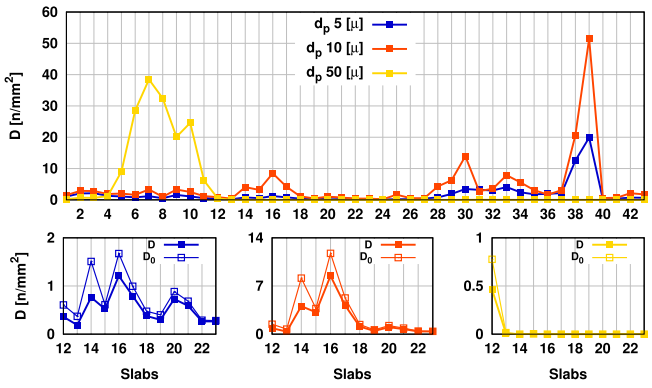

Fig. 12. Density D_i of droplets deposited upon slab i, for $\Delta p = 10$ Pa. Top: variation of D_i along the whole nasal cavity, in dependence of the thermal treatment. Bottom: differences between D_i and $D_{i,0}$ (sinuses removed), for droplet diameter of 5μm (aerosol, left), 10 μm (inhalation, center) and 50 μm (right).

except on slabs 1–3. As in the previous case, on the sinuses region the larger values of D_i and $D_{i,0}$ occur for aerosol and inhalation on the slabs 14 and 16. D_i and $D_{i,0}$ are about 0.7, 1.5 mm^{-2} for aerosol and 4, 8 mm^{-2} for inhalation on the slab 14, and 1.25, 1.6 mm^{-2} for aerosol and 8.2, 12 mm^{-2} for inhalation on the slab 16, respectively. The behavior of the largest droplets follows what has been observed for the higher pressure drop case, and the surface densities D_{12} and $D_{12,0}$ are about 0.45 and 0.8 mm^{-2}, respectively. It is worth noting that in this case $D_{i,0} > D_i$ everywhere.

4.3. Deposition fraction and effects of computational parameters

The effects of computational parameters on the droplets deposition are now assessed.

If P_d denotes the number of particles deposited on the nasal mucosa during the simulation time, and P_{tot} is the total number of particles which have entered the volume of the nasal cavity, the deposition fraction DF is defined as

$$DF = \frac{P_d}{P_{tot}}.$$

To separate the effect of droplet size and mesh resolution, Fig. 13 plots DF versus droplet size, and reveals that the impact of the grid size and inhalation rate on the deposition fraction DF is larger for small droplets. DF for the largest droplets is equal to 1, independent on breathing regime and grid size.

The dependence of DF on the mesh size is addressed again in Fig. 14, where changes in DF are observed in detail on a slab-by-slab basis. The surface density of deposited droplets is observed for aerosol, with two computational grids and two values of Δp. At the lower breathing regime we note that D_i for the finer mesh is consistently lower than D_i for the coarser mesh, except at slabs 34–37 and 39–42, i.e. close to the epiglottis and the throat section. The largest differences are observed downstream the nostrils and in the nasopharynx region. Similarly, in the higher-intensity breathing D_i on the finer mesh is everywhere lower than D_i on the coarser one, except downstream the nasopharynx and close to the throat. The region for which D_i is overestimated by the coarser mesh is wider for $\Delta p = 20$ Pa. As in the previous case, $\Delta p = 10$ Pa, we observe the largest difference in D_i between coarse and fine mesh to be located in the slabs 1, 5, 7, 9 downstream the nostrils, and in slabs 25, 27, 29, 30 in the nasopharynx region. In

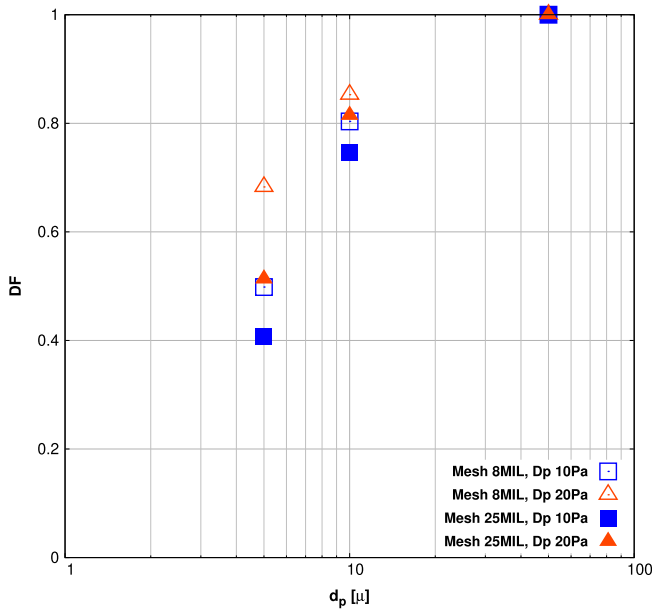

Fig. 13. Deposition fraction DF versus particle size.

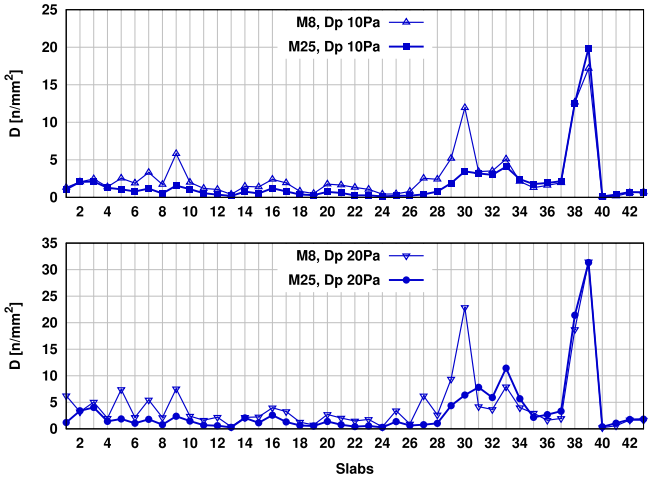

Fig. 14. Density D_i of droplets deposited upon slab i, for aerosol at $\Delta p = 10$ Pa (top) and $\Delta p = 20$ Pa (bottom): effect of the spatial resolution.

general, such differences are more evident in comparison with to the case at lower pressure difference.

5. Discussion

The flow in the nasal cavities is one where extreme geometrical complexity is accompanied by a transitional behavior: the flow is three-dimensional and unsteady, but becomes fully turbulent only in limited portions of the computational domain. The RANS approach, widely used in the CFD community due to its relatively low computational cost, is outperformed by LES at capturing the fine spatio-temporal details and at predicting droplet deposition characteristics [44,51,74]. The present case, where geometry is already strongly three-dimensional and rich with fine details, is one where the extra computational burden brought about by LES is also at its minimum. Furthermore, LES lends itself perfectly to describing unsteady effects on the time-dependent flow which develops under the steady inspiration considered here. It is experimentally shown in Ref. [75] that, for particles of the size considered in the present work, a constant flow produces deposition statistics that compare correctly with those of the full breathing cycle.

The results presented for cases h*f, see Figs. 3 and 4, evidence large velocity values close to the regions of the throat and the meati, whereas low velocity levels are observed in the paranasal sinuses. Moreover, velocity and pressure fields are non-symmetrical when observed in coronal view, owing to anatomy-related asymmetries. The high three-dimensionality of the flow field downstream of the epiglottis is revealed by the larger values of turbulent kinetic energy in Fig. 5 and is somewhat expected, as the region below the epiglottis is the most turbulent region. The smaller but still significant levels of fluctuations in the meati, where the flow is laminar or nearly so, are more interesting, and suggest the existence of an unsteady flow. This challenges the most popular modelling approaches, where the flow is considered to be either laminar and steady, or fully turbulent. Another noteworthy result is the observation, in both views of Fig. 7, of significant vortical structures in the paranasal sinuses. Despite of the low velocity values associated to such structures, this suggests the importance of carrying out CFD studies on anatomically complete models, although the issue remains open of a faithful representation of the small *ostii* from the CT scan.

The main focus of the present work is on the deposition of water droplets. The validation of such statistics is not straightforward, owing to the patient-specific nature of the present and the available literature studies. The computed deposition fraction DF can be compared to estimates via empirical correlations available in the literature, as well as to existing *in-vivo* and *in-vitro* data. A number of empirical correlations

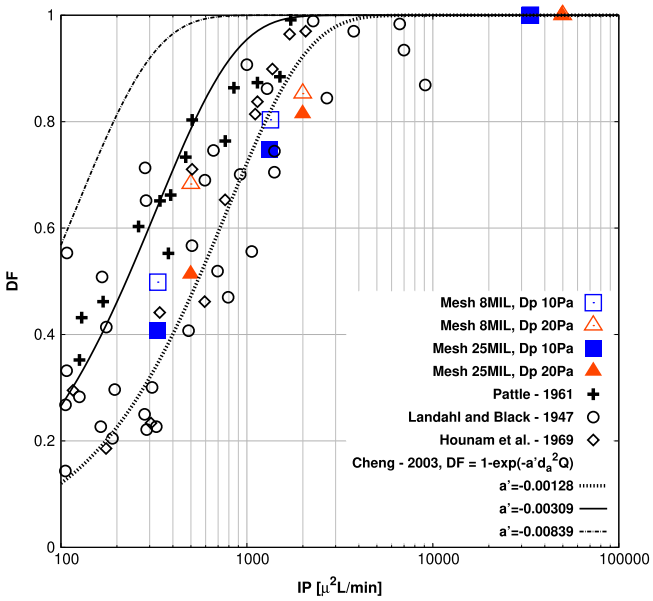

Fig. 15. Deposition fraction DF versus impaction parameter IP: comparison with *in vivo* data [9–11]. Present results are for 8 M (large open symbols) and 25 M (large filled symbols) grids, for $\Delta p = 10$ Pa (squares) and 20 Pa (triangles). The Cheng correlation [76] is also plotted, with the empirical constant a' corresponding to the maximum (dash-dotted line), mean (continuous line) and minimum (dotted line) values.

is available; one of the most widely used has been proposed by Cheng [76], and consists in the following formula:

$$DF = 1 - \exp(-a' d_a^2 Q). \tag{7}$$

In this expression Q is the inhalation rate expressed in L/min and a' is an experimentally determined constant (discussed below) possessing physical dimensions; d_a is the aerodynamic diameter of the particle, expressed in μm and defined as

$$d_a = (\rho_p/\rho_w)^{1/2} d_p,$$

where ρ_p and ρ_w denote the particle density and the water density, respectively, and d_p is the particle diameter. As it is customary in the literature, in Figs. 15 and 16 DF is plotted against the impaction parameter IP, defined as:

$$IP = d_a^2 Q$$

and compared to Eq. (7) and to published *in-vivo* and *in-vitro* data, respectively. In his study Cheng [76] observes a significant inter-study variability of DF, suggesting for the constant a' values ranging from 0.00128 to 0.00839, with a mean value of 0.00309. In Figs. 15 and 16 the lower-bound, the upper bound and the mean value of a' are used to draw the three lines. Our data agree quite well with the curve plotted with the lower value of a'. For each combination of computational parameters, the 3 droplet sizes correspond to 3 different values of IP. The largest droplets, with the largest IP values, yield a virtually complete deposition. The lower values of DF are observed, as expected, for the smaller droplets (aerosol) and the smaller inhalation rate. The larger the droplets, the larger the deposition fraction becomes for a given value of IP. Both plots also suggest an effect of the grid size: a finer grid seems to reduce DF, and the effect is more noticeable for the droplets with smaller diameter. A comparison with *in vivo* data [9–11] is proposed in Fig. 15. It shows how these data are scattered near the lower and mean curves of the Cheng correlation, hence in good agreement with our results. The comparison with *in vitro* experiments [12–15] proposed in Fig. 16 shows instead a larger variability, owing to the increased difficulty of precisely controlling the test conditions. However, with the exception of the experiment [12], all the *in-vivo* data

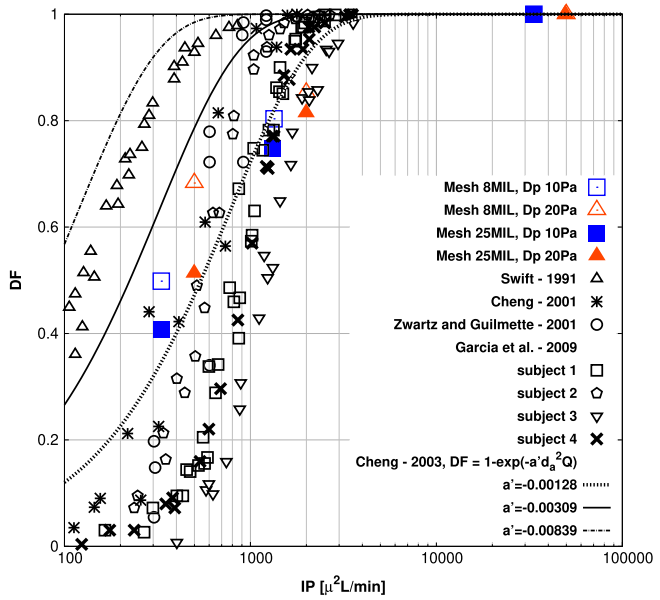

Fig. 16. Deposition fraction DF versus impaction parameter IP: comparison with *in vitro* data [12–15]. Present results are for 8 M (large open symbols) and 25 M (large filled symbols) grids, for $\Delta p = 10$ Pa (squares) and 20 Pa (triangles). The Cheng correlation [76] is also plotted, with the empirical constant a' corresponding to the maximum (dash-dotted line), mean (continuous line) and minimum (dotted line) values.

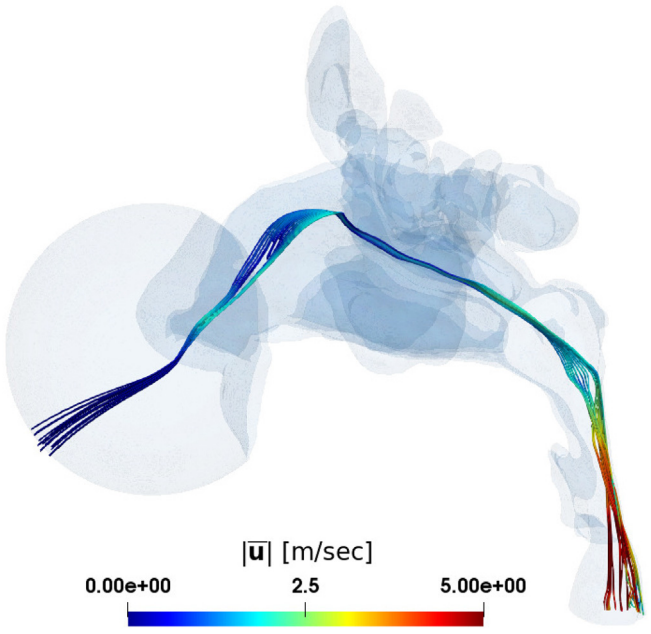

Fig. 17. Streamlines along the nasal cavity, for $\Delta p = 20$ Pa, colored by the value of the local velocity magnitude, sagittal view. The largest curvature is observed upstream of the local concentration peaks observed in Figs. 10 and 12.

follow a similar trend and fall below the mean Cheng correlation curve. Moreover, Fig. 16 and in particular the dataset by Garcia et al. [15] put in perspective the importance of inter-subject variability of the deposition fraction, which is probably one of the main reasons why the available information is so scattered.

Beyond DF, the present study has assessed the details of the droplet deposition process both quantitatively and qualitatively. The qualitative analysis has led to visually identifying the deposition pattern across the nasal cavities, whereas the quantitative assessment allowed us to capture the slab-by-slab details of the deposition in terms of surface droplets density. An extensive analysis, obtained by partitioning the computational domain in to 43 adjacent regions, extends the available literature information, see e.g. Refs. [39,44,54,55] to a higher level of detail. Figs. 10–12 suggest that inhalation produces a more efficient deposition than aerosol. Since the mass of the smaller aerosol droplet is 8 times lower, deposition via inhalation is even more effective. Moreover, a separate assessment of the surface droplet density with and without sinuses has been carried out: only few existing studies include anatomical details of the maxillary and frontal sinuses, see e.g. Refs. [77,78], and such works are not specifically focused on a in-depth analysis of regional particle deposition. The paranasal sinuses are observed to receive a non-negligible amount of water droplets, see Figs. 10 and 12. This is an interesting outcome since the importance of sinuses is well known in the development of inflammatory disorders.

Overall, both Figs. 10 and 12 indicate that particle mass has a central role in determining the deposition pattern along the nasal airways. Small droplets (aerosol and inhalation) show a tendency for localized deposition at the present values of flow rate. If the local peak around slabs 38–39 can be linked to the artificial removal of the topological connection between the epiglottis, the oral cavity and the piryform sinuses, the local peaks in regions ranging from slab 14 to 17 and after slab 28 can be related to the droplets' inertia in presence of local streamline curvature. In Fig. 17 streamlines of an instantaneous flow field are drawn along the cavity, and colored according to the value of the local velocity magnitude with the mucosal lining shown in partial transparency. It can be appreciated that significant streamline curvature is observed just upstream of the local deposition peaks mentioned above, confirming that inertia effects are responsible for the detailed deposition micro-patterns.

Limited information, see e.g. Refs. [44,54,79], is available regarding the effects of grid resolution on the deposition efficiency. In our work the dependence of DF upon the mesh size has been evaluated slab-by-slab. One could ask whether such resolution effects are related to the reduced capability of the coarser mesh to capture the flow details and the consequent larger role played by the LES model, or to the altered/degraded description of key anatomical features of the nasal cavities induced by the coarser mesh. To address this question, case haf in Table 1, presenting significant changes of DF when the mesh size is varied, has been compared with two additional cases (labeled haf- and haf+) where the computational mesh still possesses 25 M cells, but the number and size of near-wall cells is either decreased or increased to alter the mesh ability to describe the anatomy. Fig. 18 compares the slab-by-slab behavior of the three simulations. In all cases the particles injected in the domain are approximately 2×10^5; after 0.6 s 8.37×10^4 droplets have deposited on the mucosa using the baseline 25 M mesh, whereas 8.51×10^4 and 8.27×10^4 have deposited by decreasing or increasing the near-wall resolution (cases haf- and haf+). Hence a better near-wall resolution seems to slightly decrease the number of deposited droplets. However, Fig. 18 does not highlight a clear trend. It can be thus deduced that resolution-induced changes in DF can be explained by the lower degree at which the coarser meshes is able to reproduce the flow physics satisfactorily. This confirms recent information [79]

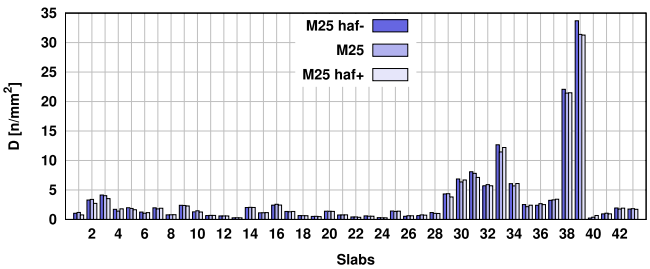

Fig. 18. Density D_i of droplets deposited upon slab i, for aerosol at $\Delta p = 20$ Pa: effect of decreasing/increasing the near-wall resolution.

obtained in the context of a laminar steady simulation, where DF has been observed to decrease with increasing mesh resolution, with an effect that becomes more evident for smaller particles.

6. Conclusions

The present work is a numerical study, based on Large-Eddy Simulation (LES), of the deposition of droplets of thermal waters upon the mucosa of the human nasal cavities, as reconstructed in detail from the CT scan of a specific patient. To the authors' knowledge, for the first time such study has been carried out with a LES, coupled with a Lagrangian approach, on a complete anatomy by using open-source software only.

The deposition pattern of droplets has been assessed both qualitatively and quantitatively for a steady inspiration. Two droplet sizes have been considered, corresponding to the thermal treatments of aerosol and inhalation. (A third, larger droplet size, loosely corresponding to the atomized nasal douche, has also been considered in the numerical experiments. However, since the douche inhaler is not present in the simulations, the results concerning the largest droplets cannot be easily extrapolated to the actual thermal treatment, although they provide a qualitative indication of the behavior of inhalation devices producing larger droplets.) The obtained results are found to be in good agreement with published *in vivo* and *in vitro* data, although a patient-specific comparison is clearly not possible.

The number of deposited particles is large enough that a 3-dimensional view of the anatomy depicting the deposition pattern has been obtained. The spatial distribution of the deposited droplets is also quantitatively studied by discretizing the computational domain into a large number of axial slabs, thus observing with unprecedented detail where along the main axis of the nasal passageways droplets show a statistical tendency to deposit. The presence in our model of the volumes of the paranasal sinuses allows the separate assessment of the amount of droplets that enter the sinuses. It should be remarked, though, that in such CT-based reconstructions the results within the sinuses should be considered with care, as the typical CT resolution precludes an accurate reconstruction of the tiny *ostii* connecting the large volume of the sinuses to the main passageways.

Remarkable differences in the deposition patterns are observed among the various thermal treatments, with larger droplets depositing on the anterior part of the nasal fossae, and the smaller ones spreading over the whole mucosa. Droplets entering the sinuses are obviously less than those depositing in the nasal fossae, confirming the importance of an accurate design for devices delivering thermal waters for treating sinusitis. Nevertheless, their number is not negligible in the present simulation where an *ad-hoc* device is absent.

The effect of the size of the computational grid and of the breathing intensities on the deposition fraction are separately investigated. It is found that the effects of the size of the computational grid is non-negligible, and its importance becomes larger for smaller droplets and at higher breathing intensities. Both observations are consistent with the increased role played by the turbulence model. Indeed, a further analysis, carried out for the smaller droplets at higher breathing intensity, has investigated a possible dependency of droplets deposition on the near-wall grid resolution, suggesting that this may not be a primary factor.

While the reliability of the present results still remains to be precisely assessed in absolute terms, we believe that the present level of detail, together with the relative accuracy implied by a LES simulation carried out on a fine enough mesh, could improve the current understanding of how the mixture of air-water droplets is distributed within the nose, thus contributing to the development of a more advanced CFD procedures for the analysis of the nasal airflow.

Acknowledgments

The present research has been founded by FoRST (Foundation for the Thermal Scientific Research), in the framework of the ATHEWADE project, "Assessment of the THermal WAter DElivery via computational fluid dynamics". The authors gratefully acknowledge the computing time obtained by the CINECA Supercomputing Center with the Iscra-C Onose-Pa project.

References

[1] G. Nappi, S. de Luca, M. Masciocchi, Medicina e clinica termale, Selecta medica (2001).
[2] HYDROGLOBE-Definition of a global framework for hydrotherapy, A FEMTEC-forst Joint Project with the Cooperation of ISMH and the Technical Support of WHO-world Health Organization, (2014).
[3] P. Braga, G. Sambataro, M. Dal Sasso, M. Culici, M. Alfieri, G. Nappi, Antioxidant effect of sulphurous thermal water on human neutrophil bursts: chemiluminescence evaluation, Respiration 75 (2) (2007) 193–201.
[4] P. Braga, M. Dal Sasso, M. Culici, A. Spallino, L. Marabini, T. Bianchi, G. Nappi, Effects of sulphurous water on human neutrophil elastase release, Ther. Adv. Respir. Dis. 4 (6) (2010) 333–340.
[5] A. Staffieri, A. Abramo, Sulphurous-arsenical-ferruginous (thermal) water inhalations reduce nasal respiratory resistance and improve mucociliary clearance in patients with chronic sinonasal disease: preliminary outcomes, Acta Otolaryngol. 127 (6) (2007) 613–617.
[6] D. Passali, E. De Corso, S. Platzgummer, C. Streitberger, S.L. Cunsolo, G. Nappi, G. Passali, L. Bellussi, Spa therapy of upper respiratory tract inflammations, Eur. Arch. Oto-Rhino-Laryngol. 270 (2) (2013) 565–570.
[7] R. Rosenfeld, J. Piccirillo, S. Chandrasekhar, I. Brook, K. Ashok Kumar, M. Kramper, R. Orlandi, J. Palmer, Z. Patel, A. Peters, S. Walsh, M. Corrigan, Clinical practice guideline: adult sinusitis, Otolaryngol. Head Neck Surg. 152 (2) (2015) S1–S39.
[8] W. Thomas, R. Harvey, L. Rudmik, P. Hwang, R. Schlosser, Distribution of topical agents to the paranasal sinuses: an evidence-based review with recommendations, Int. Forum Allergy Rhinol 3 (9) (2013) 691–703.
[9] R. Pattle, The retention of gases and particles in the human nose, Inhaled particles and vapours 1 (1961) 302–309.
[10] H. Landahl, S. Black, Penetration of airborne particulates through the human nose, J. Ind. Hyg. Toxicol. 29 (4) (1947) 269–277.
[11] R. Hounam, A. Black, M. Walsh, Deposition of aerosol particles in the nasopharyngeal region of the human respiratory tract, Nature 221 (5187) (1969) 1254.
[12] D. Swift, Inspiratory inertial deposition of aerosols in human nasal airway replicate casts: implication for the proposed ncrp lung model, Radiat. Protect. Dosim. 38 (1–3) (1991) 29–34.
[13] Y. Cheng, T. Holmes, J. Gao, R. Guilmette, S. Li, Y. Surakitbanharn, C. Rowlings, Characterization of nasal spray pumps and deposition pattern in a replica of the human nasal airway, J. Aerosol Med. 14 (2) (2001) 267–280.
[14] G. Zwartz, R. Guilmette, Effect of flow rate on particle deposition in a replica of a human nasal airway, Inhal. Toxicol. 13 (2) (2001) 109–127.
[15] G. Garcia, E. Tewksbury, B. Wong, J. Kimbell, Interindividual variability in nasal filtration as a function of nasal cavity geometry, J. Aerosol Med. Pulm. Drug Deliv. 22 (2) (2009) 139–156.
[16] M. Quadrio, C. Pipolo, S. Corti, R. Lenzi, F. Messina, C. Pesci, G. Felisati, Review of computational fluid dynamics in the assessment of nasal air flow and analysis of its limitations, Eur. Arch. Oto-Rhino-Laryngol. 271 (9) (2014) 2349–2354.
[17] G. Lamberti, F. Manara, M. Quadrio, RANS/LES/DNS simulations of the airflow in nasal cavities, DFD Meeting of the American Phyisial Society, November 22–24, Boston MA (USA), 2015.
[18] M. Quadrio, C. Pipolo, S. Corti, F. Messina, C. Pesci, A. Saibene, S. Zampini, G. Felisati, Effect of CT resolution and radiodensity threshold on the CFD evaluation of nasal airflow, Med. Biol. Eng. Comput. 54 (2016) 411–419.
[19] K. Zhao, P. Scherer, S. Hajiloo, P. Dalton, Effect of anatomy on human nasal air flow and odorant transport patterns: implications for olfaction, Chem. Senses 29 (5) (2004) 365–379.
[20] K. Zhao, P. Dalton, G. Yang, P. Scherer, Numerical modeling of turbulent and laminar airflow and odorant transport during sniffing in the human and rat nose, Chem. Senses 31 (2) (2005) 107–118.
[21] S. Naftali, M. Rosenfeld, M. Wolf, D. Elad, The air-conditioning capacity of the human nose, Ann. Biomed. Eng. 33 (4) (2005) 545–553.
[22] D. Elad, S. Naftali, M. Rosenfeld, M. Wolf, Physical stresses at the air-wall interface of the human nasal cavity during breathing, J. Appl. Physiol. 100 (3) (2006) 1003–1010.
[23] K. Vogt, G. Bachmann-Harildstad, A. Lintermann, A. Nechyporenko, F. Peters, K. Wernecke, The New Agreement of the International Riga Consensus Conference on Nasal Airway Function tests., Rhinology.
[24] H. Calmet, A. Gambaruto, A. Bates, M. Vázquez, G. Houzeaux, D. Doorly, Large-scale CFD simulations of the transitional and turbulent regime for the large human airways during rapid inhalation, Comput. Biol. Med. 69 (2016) 166–180.
[25] K. Zhao, J. Jiang, What is normal nasal airflow? a computational study of 22 healthy adults, Int. Forum Allergy Rhinol 4 (6) (2014) 435–446.
[26] A.J. Bates, D.J. Doorly, R. Cetto, H. Calmet, A. Gambaruto, N. Tolley, G. Houzeaux, R. Schroter, Dynamics of airflow in a short inhalation, J. R. Soc. Interface 12 (102)

(2015) 20140880.
[27] J. Rhee, S. Pawar, G. Garcia, J. Kimbell, Toward personalized nasal surgery using computational fluid dynamics, Arch. Facial Plast. Surg. (2011) E1–E6.
[28] J. Rhee, D. Cannon, D. Frank, J. Kimbell, Role of virtual surgery in preoperative planning: assessing the individual components of functional nasal airway surgery, Arch. Facial Plast. Surg. 14 (5) (2012) 354–359.
[29] K. Hemtiwakorn, V. Mahasitthiwat, S. Tungjitkusolmun, K. Hamamoto, C. Pintavirooj, Patient-specific aided surgery approach of deviated nasal septum using computational fluid dynamics, IEEJ T. Electr. Electr 10 (3) (2015) 274–286.
[30] B. Hariri, J. Rhee, G. Garcia, Identifying patients who may benefit from inferior turbinate reduction using computer simulations, Laryngoscope 125 (12) (2015) 2635–2641.
[31] T. Nomura, M. Ushio, K. Kondo, T. Yamasoba, Effects of nasal septum perforation repair surgery on three-dimensional airflow: an evaluation using computational fluid dynamics, Eur. Arch. Oto-Rhino-Laryngol. 272 (11) (2015) 3327–3333.
[32] G. Xiong, J. Zhan, K. Zuo, J. Li, L. Rong, G. Xu, Numerical flow simulation in the post-endoscopic sinus surgery nasal cavity, Med. Biol. Eng. Comput. 46 (2008) 1161–1167.
[33] J. Xi, J. Yuan, X. Si, J. Hasbany, Numerical optimization of targeted delivery of charged nanoparticles to the ostiomeatal complex for treatment of rhinosinusitis, Int. J. Nanomed. 10 (2015) 4847.
[34] K. Inthavong, Z. Tian, J. Tu, W. Yang, C. Xue, Optimising nasal spray parameters for efficient drug delivery using computational fluid dynamics, Comput. Biol. Med. 38 (6) (2008) 713–726.
[35] X. Tong, J. Dong, Y. Shang, K. Inthavong, J. Tu, Effects of nasal drug delivery device and its orientation on sprayed particle deposition in a realistic human nasal cavity, Comput. Biol. Med. 77 (2016) 40–48.
[36] A. Kishore, L. Blake, C. Wang, S. Ba, G. Gross, Evaluating the effect of sinex®(0.05% oxymetazoline) nasal spray on reduction of nasal congestion using computational fluid dynamics, J. Biomech. Eng. 137 (8) (2015) 081011.
[37] Z. Tian, K. Inthavong, J. Tu, Deposition of inhaled wood dust in the nasal cavity, Inhal. Toxicol. 19 (14) (2007) 1155–1165.
[38] H. Tang, J. Tu, H. Li, B. Au-Hijleh, C. Xue, C. Li, Dynamic analysis of airflow features in a 3d real-anatomical geometry of the human nasal cavity, 15th Australasian Fluid Mechanics ConferenceAustralia, 2004, pp. 80–83.
[39] J. Schroeter, J. Kimbell, B. Asgharian, Analysis of particle deposition in the turbinate and olfactory regions using a human nasal computational fluid dynamics model, J. Aerosol Med. 19 (3) (2006) 301–313.
[40] K. Shanley, P. Zamankhan, G. Ahmadi, P. Hopke, Y. Cheng, Numerical simulations investigating the regional and overall deposition efficiency of the human nasal cavity, Inhal. Toxicol. 20 (12) (2008) 1093–1100.
[41] H. Shi, C. Kleinstreuer, Z. Zhang, Modeling of inertial particle transport and deposition in human nasal cavities with wall roughness, J. Aerosol Sci. 38 (4) (2007) 398–419.
[42] T. Martonen, Z. Zhang, G. Yue, C. Musante, 3-d particle transport within the human upper respiratory tract, J. Aerosol Sci. 33 (8) (2002) 1095–1110.
[43] X. Si, J. Xi, J. Kim, Effect of laryngopharyngeal anatomy on expiratory airflow and submicrometer particle deposition in human extrathoracic airways, O. J. Fluid Dynam. 3 (4) (2013).
[44] Y. Liu, E. Matida, J. Gu, M. Johnson, Numerical simulation of aerosol deposition in a 3-D human nasal cavity using RANS, RANS/EIM, and LES, J. Aerosol Sci. 38 (7) (2007) 683–700.
[45] Y. Zhang, W. Finlay, E. Matida, Particle deposition measurements and numerical simulation in a highly idealized mouth–throat, J. Aerosol Sci. 35 (7) (2004) 789–803.
[46] E. Matida, W. Finlay, C. Lange, B. Grgic, Improved numerical simulation of aerosol deposition in an idealized mouth–throat, J. Aerosol Sci. 35 (1) (2004) 1–19.
[47] Z. Zhang, C. Kleinstreuer, C. Kim, Micro-particle transport and deposition in a human oral airway model, J. Aerosol Sci. 33 (12) (2002) 1635–1652.
[48] K. Stapleton, E. Guentsch, M. Hoskinson, W. Finlay, On the suitability of k–ε turbulence modeling for aerosol deposition in the mouth and throat: a comparison with experiment, J. Aerosol Sci. 31 (6) (2000) 739–749.
[49] J. Xi, X. Si, J. Kim, A. Berlinski, Simulation of airflow and aerosol deposition in the nasal cavity of a 5-year-old child, J. Aerosol Sci. 42 (3) (2011) 156–173.
[50] K. Inthavong, Z. Tian, H. Li, J. Tu, W. Yang, C. Xue, C. Li, A numerical study of spray particle deposition in a human nasal cavity, Aerosol Sci. Technol. 40 (11) (2006) 1034–1045.
[51] E. Matida, W. Finlay, M. Breuer, C. Lange, Improving prediction of aerosol deposition in an idealized mouth using large-eddy simulation, J. Aerosol Med. 19 (3) (2006) 290–300.
[52] X. Chen, H. Lee, V. Chong, D. Wang, Assessment of septal deviation effects on nasal air flow: a computational fluid dynamics model, Laryngoscope 119 (2009) 1730–1736.
[53] G. Mylavarapu, S. Murugappan, M. Mihaescu, M. Kalra, S. Khosla, E. Gutmark, Validation of computational fluid dynamics methodology used for human upper airway flow simulations, J. Biomech. 42 (10) (2009) 1553–1559.
[54] Y. Liu, E. Matida, M. Johnson, Experimental measurements and computational modeling of aerosol deposition in the carleton-civic standardized human nasal cavity, J. Aerosol Sci. 41 (6) (2010) 569–586.
[55] J. Xi, J. Kim, X. Si, Effects of nostril orientation on airflow dynamics, heat exchange, and particle depositions in human noses, Eur. J. Mech. B Fluids 55 (2016) 215–228.
[56] A. Farnoud, X. Cui, I. Baumann, E. Gutheil, Numerical analysis of the flow and particles pattern in the human nasal cavity, in: ICMF Congress, Firenze (I), May 22-27, 2016.
[57] H. Weller, G. Tabor, H. Jasak, C. Fureby, A tensorial approach to computational continuum mechanics using object-oriented techniques, Comput. Phys. 12 (6) (1998) 620–631.
[58] A. Fedorov, R. Beichel, J. Kalpathy-Cramer, J. Finet, J.-C. Fillion-Robin, S. Pujol, C. Bauer, D. Jennings, F. Fennessy, M. Sonka, J. Buatti, S. Aylward, J. Miller, S. Pieper, R. Kikinis, 3D slicer as an image computing platform for the quantitative imaging network, J. Magn. Reson. Imag. 30 (9) (2012) 22770690.
[59] S. Pope, Turbulent Flows, IOP Publishing, 2001.
[60] J. Smagorinsky, General circulation experiments with the primitive equations: I. the basic experiment, Mon. Weather Rev. 91 (3) (1963) 99–164.
[61] E. Van Driest, On turbulent flow near a wall, J. Aeronaut. Sci. 23 (11) (1956) 1007–1011.
[62] C. Crowe, J. Schwarzkopf, M. Sommerfeld, Y. Tsuji, Multiphase Flows with Droplets and Particles, CRC press, 2011, p. 509.
[63] J. Ferziger, M. Peric, Computational Methods for Fluid Dynamics, Springer, Berlin, 2013.
[64] K. Zhao, P. Dalton, G. Yang, P. Scherer, Numerical modeling of turbulent and laminar airflow and odorant transport during sniffing in the human and rat nose, Chem. Senses 31 (2006) 107–118.
[65] D. Wang, H. Lee, R. Gordon, Impacts of fluid dynamics simulation in study of nasal airflow physiology and pathophysiology in realistic human three-dimensional nose models, Clin. Exp. Otorhinolaryngol 5 (4) (2012) 181–187.
[66] E. Bilgen, P. Arbour, P. Turik, On the Resistance of Air Flow through the Nose, New York: ASME Pub., United Eng.Cent.
[67] R. Hooper, Forced inspiratory nasal flow-volume curves: a simple test of nasal airflow, Mayo Clin. Proc. 76 (10) (2001) 990–994.
[68] X. Liu, W. Yan, Y. Liu, Y. Choy, Y. Wei, Numerical investigation of flow characteristics in the obstructed realistic human upper airway, Computational and mathematical methods in medicine (2016) 3181654.
[69] P. Djupesland, Nasal drug delivery devices: characteristics and performance in a clinical perspective–a review, Drug delivery and translational research 3 (1) (2013) 42–62.
[70] J. Mitchell, M. Nagel, Particle size analysis of aerosols from medicinal inhalers, KONA Powder and Particle Journal 22 (2004) 32–65.
[71] C. Reisner, R. Katial, B. Bartelson, A. Buchmeir, L. Rosenwasser, H. Nelson, Characterization of aerosol output from various nebulizer/compressor combinations, Ann. Allergy Asthma Immunol. 86 (5) (2001) 566–574.
[72] J. Jeong, F. Hussain, On the identification of a vortex, J. Fluid Mech. 285 (1995) 69–94.
[73] J. Ahrens, B. Geveci, C. Law, C. Hansen, C. Johnson, Paraview: an End-user Tool for Large-data Visualization, the Visualization Handbook 717.
[74] S. Jayaraju, M. Brouns, C. Lacor, B. Belkassem, S. Verbanck, Large eddy and detached eddy simulations of fluid flow and particle deposition in a human mouth–throat, J. Aerosol Sci. 39 (10) (2008) 862–875.
[75] S. Häußermann, A. Bailey, M. Bailey, G. Etherington, M. Youngman, The influence of breathing patterns on particle deposition in a nasal replicate cast, J. Aerosol Sci. 33 (2002) 923–933.
[76] Y. Cheng, Aerosol deposition in the extrathoracic region, Aerosol Sci. Technol. 37 (8) (2003) 659–671.
[77] T. Henn, G. Thäter, W. Dörfler, H. Nirschl, M. Krause, Parallel dilute particulate flow simulations in the human nasal cavity, Comput. Fluids 124 (2016) 197–207.
[78] Q. Ge, K. Inthavong, J. Tu, Local deposition fractions of ultrafine particles in a human nasal-sinus cavity cfd model, Inhal. Toxicol. 24 (8) (2012) 492–505.
[79] D. Frank-Ito, M. Wofford, J. Schroeter, J. Kimbell, Influence of mesh density on airflow and particle deposition in sinonasal airway modeling, J. Aerosol Med. Pulm. Drug Deliv. 29 (1) (2015) 46–56.